

# Towards Efficient PCSEL Design: A Data-Driven Approach for Design Insights

HAI HUANG,<sup>1,2</sup> ZITENG XU,<sup>1,2</sup> AND ZHAOYU ZHANG<sup>1,2,\*</sup>

<sup>1</sup>*School of Science and Engineering, The Chinese University of Hong Kong, Shenzhen, Guangdong 518172, China.*

<sup>2</sup>*Guangdong Key Laboratory of Optoelectronic Materials and Chips and Shenzhen Key Lab of Semiconductor Lasers, School of Science and Engineering, The Chinese University of Hong Kong, Shenzhen, Guangdong 518172, China.*

\*zhangzy@cuhk.edu.cn

**Abstract:** We present a data-driven design approach for photonic crystals to achieve high efficiency in photonic crystal surface-emitting lasers (PCSELs). By discretizing the photonic crystal structure into a grid, we enable the generation of arbitrary lattice designs. Multiple fully connected layers combined with a position embedding module extract essential features from the photonic crystal designs, while coupled-wave theory (CWT) is used to evaluate the efficiency based on the ratio of surface-emitting to edge-emitting resonant modes. The model achieves high prediction accuracy, with Pearson correlation coefficients of 0.88 for SEE and 0.78 for the log-transformed Q. Additionally, we perform Shapley value analysis to identify the most important Fourier coefficients, providing insights into the factors that impact the performance of PCSEL designs. Our work speeds up the design process and offers valuable guidance for optimizing high-performance PCSELs, supporting the development of fully photonic design automation (PDA).

## 1. Introduction

Photonic crystal surface-emitting lasers (PCSELs) have attracted significant interest due to their potential across a wide range of applications, including light detection and ranging (LIDAR) systems, laser processing, and optical communications [1–4]. These devices offer the unique advantage of operating in a surface-emitting configuration, which provides several benefits over traditional semiconductor lasers, such as edge-emitting lasers (EELs) and vertical cavity surface-emitting lasers (VCSELs). These benefits include high output power, excellent beam quality, an ultra-small divergence angle, and single-mode operation [1, 5, 6]. Despite these advantages, traditional methods for designing photonic crystals often rely on trial-and-error or parameter sweep approaches [4, 7–9]. These methods can be both time-consuming and computationally expensive, making it difficult to efficiently explore the vast design space of PCSELs.

Data-driven approaches have gained traction in the field of photonics, as they provide a more efficient alternative for design optimization [10, 11]. These methods leverage machine learning models to explore complex design spaces and identify optimal solutions without the need for exhaustive simulations. By applying these techniques, the design process can be significantly accelerated, and the computational burden reduced [12, 13]. However, most existing approaches focus on general optimization rather than providing insights into the specific features of photonic crystals that drive performance, which limits their applicability to high-efficiency PCSEL design.

In this study, we propose a novel data-driven approach tailored specifically for the design of PCSELs. By discretizing the photonic crystal structure into a grid, our method facilitates the generation of a wide variety of lattice configurations, significantly expanding the range of possible designs. One of the key features of our approach is the use of Neural Networks (NNs) [14], a type of machine learning model well-suited for identifying intricate patterns and relationships within complex datasets. NNs excel at extracting essential features from the photonic crystal

structures, such as Fourier coefficients, which serve as a compact representation of the structure’s key characteristics. By leveraging NNs, we are able to capture critical features, such as symmetry and destructive interactions, in double-lattice [8] or triple-lattice photonic crystals [15], that strongly influence laser performance.

Additionally, we employ coupled-wave theory (CWT) [16–18] to evaluate the performance of the PCSEL designs. CWT offers a reliable and efficient method for calculating the ratio of surface-emitting to edge-emitting power for different resonant modes. By utilizing CWT, we are able to dramatically reduce the computational time for each design, enabling rapid evaluation of finite-size PCSELS. The synergy between NNs and CWT allows us to accelerate the design and optimization process while maintaining high accuracy in efficiency predictions.

In addition to the performance prediction, we perform Shapley value analysis to assess the relative importance of each Fourier coefficient in determining the efficiency of PCSEL designs. Shapley values, derived from cooperative game theory [19], offer a quantitative measure of each input parameter’s impact on the model’s output. This analysis reveals the most influential features of the photonic crystal structure, providing valuable insights into the key factors that drive the performance of PCSELS.

By combining data-driven design methods, CWT, and Shapley value analysis, our approach not only speeds up the design process but also offers a deeper understanding of the structural features that impact PCSEL efficiency. This method provides a powerful tool for optimizing PCSELS and offers the potential for greater automation in photonic device design. In the following sections, we describe the implementation of our approach, present the results from model training and testing, and discuss the insights gained from Shapley value analysis.

## 2. Methods

### 2.1. Photonic crystal simulation

To design arbitrary photonic crystals, we first define a random filling factor ( $FF$ ), which determines the ratio of high and low dielectric constant materials within the photonic crystal and is expressed as  $FF = S_{\text{low dielectric}}/S_{\text{high dielectric}}$ . The unit cell of the photonic crystal is discretized into an  $n \times n$  grid (for a square lattice). For each grid cell, a value  $z = f(x, y)$  is generated, with  $f(x, y)$  defining the spatial distribution. This value is compared with a threshold based on the filling factor ( $FF$ ). If the generated value exceeds the threshold, the grid cell is assigned to a high dielectric constant material (e.g., GaAs). Otherwise, it is assigned to a low dielectric constant material (e.g., air).

For the numerical analysis of the photonic crystal, we apply Coupled-Wave Theory (CWT) to analyze a square lattice structure. In this approach, we consider the propagation of four basic waves along the  $x$ - and  $y$ -directions relative to the photonic crystal. The coupling between these waves can be described using the coupling matrix  $\mathbf{C}$ , which can be expressed in the following form:

$$\mathbf{C} = \mathbf{C}_{1D} + \mathbf{C}_{\text{rad}} + \mathbf{C}_{2D} \quad (1)$$

where  $\mathbf{C}_{1D}$ ,  $\mathbf{C}_{\text{rad}}$ , and  $\mathbf{C}_{2D}$  are the coupling matrices for the 1D back-diffraction feedback, radiation waves coupling, and 2D diffraction feedback, respectively. They are given by the following expressions:

$$\mathbf{C}_{1D} = \begin{pmatrix} 0 & \kappa_{2,0} & 0 & 0 \\ \kappa_{-2,0} & 0 & 0 & 0 \\ 0 & 0 & 0 & \kappa_{0,2} \\ 0 & 0 & \kappa_{0,-2} & 0 \end{pmatrix} \quad (2)$$

$$\mathbf{C}_{\text{rad}} = \begin{pmatrix} \zeta_{1,0}^{(1,0)} & \zeta_{1,0}^{(-1,0)} & 0 & 0 \\ \zeta_{-1,0}^{(1,0)} & \zeta_{-1,0}^{(-1,0)} & 0 & 0 \\ 0 & 0 & \zeta_{0,1}^{(0,1)} & \zeta_{0,1}^{(0,-1)} \\ 0 & 0 & \zeta_{0,-1}^{(0,1)} & \zeta_{0,-1}^{(0,-1)} \end{pmatrix} \quad (3)$$

$$\mathbf{C}_{2\text{D}} = \begin{pmatrix} \chi_{y,1,0}^{(1,0)} & \chi_{y,1,0}^{-1,0} & \chi_{y,1,0}^{(0,1)} & \chi_{y,1,0}^{0,-1} \\ \chi_{y,-1,0}^{(1,0)} & \chi_{y,-1,0}^{-1,0} & \chi_{y,-1,0}^{(0,1)} & \chi_{y,-1,0}^{0,-1} \\ \chi_{x,0,1}^{(1,0)} & \chi_{x,0,1}^{-1,0} & \chi_{x,0,1}^{(0,1)} & \chi_{x,0,1}^{0,-1} \\ \chi_{x,0,-1}^{(1,0)} & \chi_{x,0,-1}^{-1,0} & \chi_{x,0,-1}^{(0,1)} & \chi_{x,0,-1}^{0,-1} \end{pmatrix} \quad (4)$$

For detailed calculations of the elements in the matrices of Eq. (2), Eq. (3) and Eq. (4), please refer to Ref. [16, 18].

Thus, we can describe the four basic waves in the photonic crystal as:

$$\left( \delta + i \frac{\alpha_r}{2} \right) \begin{pmatrix} R_x \\ S_x \\ R_y \\ S_y \end{pmatrix} = \mathbf{C} \begin{pmatrix} R_x \\ S_x \\ R_y \\ S_y \end{pmatrix} + i \begin{pmatrix} \partial R_x / \partial x \\ -\partial S_x / \partial x \\ \partial R_y / \partial y \\ -\partial S_y / \partial y \end{pmatrix} \quad (5)$$

where  $\delta$  is the frequency detuning which can be expressed as  $\delta = (\beta^2 - \beta_0^2) / 2\beta_0 \simeq \beta - \beta_0 = n_{eff}(\omega - \omega_B) / c$ , with  $\omega$  being the frequency of the resonant mode and  $\omega_B$  being the Bragg frequency. The parameter  $\alpha_r$  is the total optical radiation loss of the resonant mode. The  $R_x$ ,  $S_x$ ,  $R_y$ , and  $S_y$  are the amplitudes of the four basic waves. The partial derivatives in the right-hand side of Eq. (5) are the spatial derivatives of the amplitudes of the four basic waves.

Applying the boundary conditions  $R_x(0, y) = S_x(L, y) = R_y(x, 0) = S_y(x, L) = 0$  for a finite-size  $L \times L$  square-lattice photonic crystal, we can solve Eq. (5) to obtain the spatial distribution of four basic waves. We can then calculate the optical power of the surface-emitting and edge-emitting, and derive the efficiency of the PCSEL. The optical power of all stimulated emission, surface-emitting and emitting can be expressed as:

$$P_{\text{stim}} = \alpha_r \iint_0^L (|R_x|^2 + |S_x|^2 + |R_y|^2 + |S_y|^2) dx dy \quad (6)$$

$$P_{\text{edge}} = \int_0^L (|R_x|^2 + |S_x|^2)|_{x=0,L} dy + \int_0^L (|R_y|^2 + |S_y|^2)|_{y=0,L} dx \quad (7)$$

$$P_{\text{surface}} = 2\Im(\kappa_v) \iint_0^L (|\xi_{-1,0} R_x + \xi_{1,0} S_x|^2 + |\xi_{0,-1} R_y + \xi_{0,1} S_y|^2) dx dy \quad (8)$$

Note that, in Eq. (8),  $\kappa_v$  is a term associated with radiation waves coupling and  $\xi$  is Fourier coefficient (seeing Ref. [17]).

To evaluate the efficiency of the designed PCSEL, we consider the ratio of surface-emitting power to the stimulated emission power as surface-emitting efficiency ( $SEE$ ). Since we are designing a surface-emitting laser, a higher ratio of  $SEE = P_{\text{surface}} / P_{\text{stim}}$  indicates higher efficiency of the laser. Specifically, the efficiency is enhanced when the surface-emitting power is maximized relative to the total stimulated emission, which leads to greater power extraction through the surface of the device. This ratio can be used as a key performance indicator for optimizing the photonic crystal structure for high-efficiency laser operation.

In addition to surface-emitting efficiency, the value of the quality factor  $Q$  is also an important metric for evaluating the performance of PCSELS. The quality factor is defined as the ratio of the energy stored in the cavity to the energy lost per cycle, and is given by  $Q = \frac{2\pi/a}{\alpha_r}$ , where  $a$  is the lattice constant of the photonic crystal. A high quality factor indicates low cavity loss and high energy storage, which are essential for low-threshold lasing. Therefore, the quality factor is also a key result that we need to extract from the model to ensure the laser operates at its optimal performance. To handle the large variation in the value of  $Q$  (ranging from  $10^3$  to  $10^5$ ), we trained the model to predict  $\log Q$  instead of  $Q$  directly. This transformation reduces the dynamic range of the target values, thereby stabilizing the training process and improving convergence. After prediction, the final  $Q$  value is obtained by taking the exponential of the model output. This approach ensures that the model captures the underlying pattern more effectively while minimizing sensitivity to extreme variations in  $Q$ .

## 2.2. Neural network architecture

We developed a fully connected neural network (shown in Figure 1), to predict  $SEE$  and  $\log Q$  of PCSEL designs. The model begins by 1024 input grid, which represents the real and imaginary parts of the Fourier coefficients ( $\xi_{m,n}^X$ , where  $X \in \{R, I\}$ ) of the discretized photonic crystal structure. A learnable positional embedding [20] ( $PE_{m,n}^R$  and  $PE_{m,n}^I$ ) is then added to this flattened input to help capture spatial information. We set  $PE_{m,n}^R = PE_{m,n}^I$  to ensure that the real and imaginary parts of the Fourier coefficients have the same positional embedding. For simplicity and to reduce redundancy, we only retain one of the pairings of  $\xi_{m,n}^X$  and  $\xi_{-m,-n}^X$  in our analysis. This is because these coefficients are complex conjugates of each other and represent the same input. By removing the conjugate pair, we avoid duplicating the information, ensuring more efficient processing without loss of relevant data.

The network consists of four fully connected layers with 1024, 512, 256, and 64 neurons, respectively. Each layer is followed by a Parametric ReLU (PReLU) activation function, which introduces nonlinearity and aids in learning complex patterns. Finally, an output layer with a single neuron predicts  $SEE$  and  $\log Q$ . Note that a sigmoid activation function is applied to the output for  $SEE$  to ensure its value is constrained within the range  $(0, 1)$ .

This architecture is designed to effectively learn the mapping between the grid-based representation of the photonic crystal and its performance, enabling accurate prediction of the laser's performance.

## 2.3. Generation of train and test dataset

The dataset for training and testing was generated using a Python-based simulation pipeline. In this process, random parameters are first selected to define the characteristics of three holes in the photonic crystal unit cell. For each hole, random center positions, standard deviations, and orientation angles are generated. A two-dimensional Gaussian function is then used to produce a spatial distribution for each hole, and these distributions are summed to form a composite sample array. The final resulting dielectric array is reshaped and averaged into a  $32 \times 32$  grid.

The simulation function is subsequently called with the generated dielectric array and a solver instance. This function performs optical simulations based on coupled-wave theory (CWT) and finite element method (FEM) analysis, and returns key performance metrics such as the  $SEE$  and quality factor  $Q$ , and other relevant parameters. We adopt the epitaxial structure outlined in Table 1, with the Bragg wavelength fixed at 980 nm. To ensure consistency with the finite-size PCSELS, the photonic crystal's lateral dimension  $L$  is chosen to be as close as possible to  $200 \mu m$ , while maintaining an integer multiple of the crystal period. The photonic crystal unit cells are discretized using a  $17 \times 17$  grid to capture the structural details accurately. The results are then written to a NPZ file [21], which serves as the dataset for further model training and testing. This iterative process continues until an external stop signal is detected, thereby

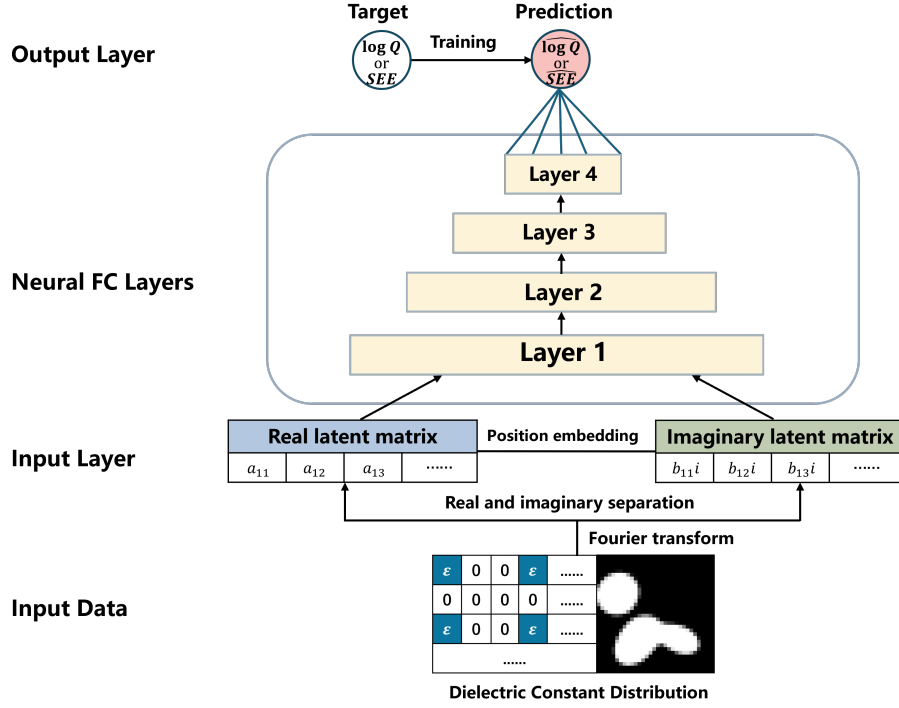


Fig. 1. The architecture of the neural network used for predicting the efficiency of PCSELS. The real latent matrix  $a$  corresponds to the Fourier coefficients  $\xi_{m,n}^R$ , while the imaginary latent matrix  $b$  represents the Fourier coefficients  $\xi_{m,n}^I$ . The network consists of four layers (Layer 1 to Layer 4), with each layer learning to map the input coefficients to the final prediction of either  $\log Q$  or  $SEE$ .

building a comprehensive dataset of photonic crystal designs. Finally, our dataset consists of 200k simulation results, ensuring a diverse and representative set of samples for training robust machine learning models.

The epitaxial structure used in this work, as shown in Table 1, serves as an example for the design of the PCSEL. The choice of epitaxial layers mainly impacts the Green's function and the confinement factor of the photonic crystal ( $\Gamma_{\text{PhC}}$ ) within the framework of CWT. However, since the primary focus of this work is on the design of the photonic crystal structure itself, the specific epitaxial layers chosen do not significantly affect the overall performance. Furthermore, the methodology proposed here can be easily adapted to other epitaxial structures, making the design approach flexible for various PCSELS epitaxial structures.

#### 2.4. Shaply values analysis

We employed Shapley values, a game-theoretic approach for interpreting machine learning models [19], to evaluate the influence of each input on the neural network model's predictions. Since our input features are represented as the real and imaginary parts of the Fourier series coefficients of the photonic crystal structure, we computed Shapley values for each component separately to quantify their contribution to the predicted  $SEE$  and  $Q$ . The Shapley value analysis was implemented using the SHAP library [22]. This approach helps us understand which Fourier coefficients most significantly affect the surface-emitting efficiency and quality factor, providing insight into the design of PCSELS.

Table 1. Epitaxial structure of the PCSEL in this work.

Layer	Material	Thickness ( $\mu\text{m}$ )	Refractive Index
Photonic Crystal	p-GaAs/Air	0.35	3.4826/1
Waveguide	p-GaAs	0.08	3.4826
Electron Blocking Layers	p-AlGaAs	0.025	3.2806
Active Region	InGaAs/AlGaAs	0.116	3.3944
n-cladding	n-AlGaAs	2.11	3.2441
n-substrate	n-GaAs	-	3.4826

### 3. Results and discussion

#### 3.1. Model training and testing

We trained a fully connected neural network to predict key performance metrics of photonic crystal surface-emitting laser (PCSEL) designs based on the generated dataset. The dataset, was split into 190k samples for training and 10k samples for testing. The model was trained using the Adam optimizer and training process was run for up to 100 epochs, with early stopping based on the validation loss to prevent overfitting (shown in Figure 2 (a) and (d)). Train epoch finally stopped at about 45 epochs. We evaluated the model’s performance on the test set using the Pearson correlation coefficient as the primary metric. Pearson’s correlation coefficient is used to evaluate the linear relationship between predicted and actual values, providing insight into the model’s predictive accuracy. The results are summarized in Table 2, which shows a high correlation between the predicted and actually simulated efficiency values. In Figure 2 (b) and (e), we present the test results for  $SEE$  and  $\log Q$ , respectively. These results demonstrate that the model effectively captures the key performance characteristics of PCSEL designs, with relatively high prediction accuracy. The error distribution for the training results of  $SEE$  and  $\log Q$  is shown in Figure 2 (c) and (f), respectively. About 80% of the predictions fall within a range of  $\pm 0.14$  for  $SEE$  and  $\pm 0.15$  for  $\log Q$ , indicating that the model produces accurate estimates with minimal deviation from the simulated values.

Table 2. Performance metrics of the NN model on the test dataset for predicting the quality factor  $\log Q$  and surface-emitting efficiency  $SEE$ .

Metric	Pearson Correlation Coefficient (and p-value)	RMSE	$R^2$
$SEE$	0.780 (p < 0.001)	0.144	0.595
$\log Q$	0.887 (p < 0.001)	0.140	0.784

As shown in Table 2 these results demonstrate that the neural network model effectively captures the key performance characteristics of PCSEL designs. The Pearson correlation coefficients which means the linear relationship between predicted and actual values, are 0.780 for  $SEE$  and 0.887 for  $\log Q$ . These high correlation values indicate that the model has strong predictive capability. The relatively low RMSE (Root of Mean Square Error) values further suggest that the model produces accurate estimates with a minimal deviation from the simulated values. We also calculated the coefficient of determination ( $R^2$ ) to evaluate the proportion of variance in the data that is explained by the model. An  $R^2$  value closer to 1 indicates that the model explains a larger

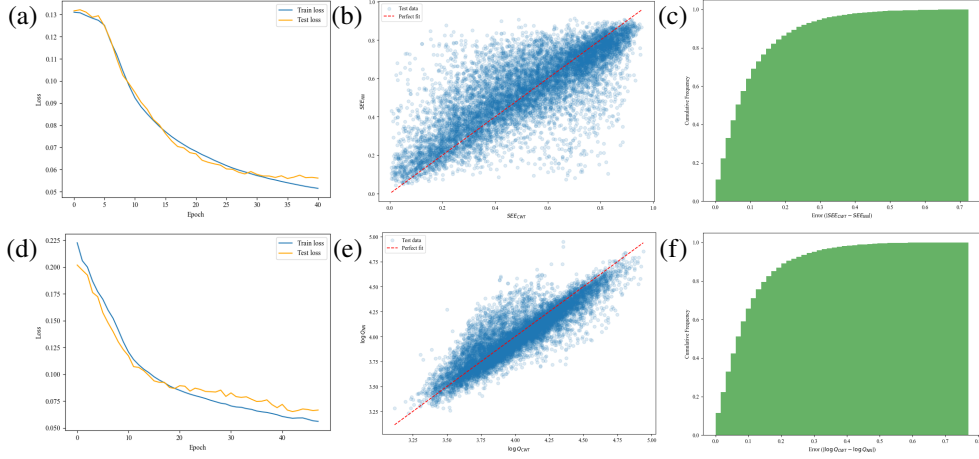


Fig. 2. Training results for  $SEE$  and  $Q$  models. (a) and (d) show the learning curves for surface-emitting efficiency ( $SEE$ ) and log-transformed quality factor ( $\log Q$ ) during training, respectively. (b) and (e) display the corresponding test results for  $SEE$  and  $\log Q$ , while (c) and (f) present the error distribution for the training results of  $SEE$  and  $\log Q$ , respectively.

portion of the variance in the data, confirming its predictive power. In our results, the  $R^2$  values of 0.595 for  $SEE$  and 0.784 for  $\log Q$  confirm that the model explains a substantial portion of the variance in the data. These findings highlight the potential of data-driven approaches for accelerating the optimization of PCSEL designs, reducing reliance on computationally expensive simulations while maintaining high prediction accuracy.

### 3.2. Shaply values analysis

To gain insights into the relative importance of different input features in determining the efficiency of PCSEL designs, we conducted a Shapley value analysis (on 500 randomly selected samples from the test dataset). The results of this analysis are shown in Figure 3, which illustrates the contribution of each Fourier coefficient to the predicted  $SEE$  and  $\log Q$ . The Shapley values provide a quantitative measure of the impact of each input parameter on the model's output, revealing the most influential features in the photonic crystal structure.

For  $SEE$ , the Fourier coefficients  $\xi_{1,0}^R$  and  $\xi_{0,1}^R$  have the most significant influence. Higher deviation values of these coefficients (further from the mean) lead to an increase in  $SEE$ , while values closer to the mean result in a decrease in  $SEE$ . For  $\log Q$ , the trend is reversed. Higher deviation values of  $\xi_{1,0}^R$  and  $\xi_{0,1}^R$  lead to a decrease in  $\log Q$ , while values closer to the mean result in an increase in  $\log Q$ . This behavior is due to the direct relationship between  $\xi_{1,0}^R$  and  $\xi_{0,1}^R$  with radiation coupling. When these coefficients deviate more from the mean, they increase the radiation loss, thereby decreasing  $\log Q$ , while more moderate values allow for better confinement and lower radiation loss.

The  $\xi_{0,0}^R$ , which corresponds to the average dielectric constant of the photonic crystal layer, also has a notable influence on both  $SEE$  and  $\log Q$ .  $\xi_{0,0}^R$  shows a generally positive correlation with both  $SEE$  and  $\log Q$ . This suggests that higher values of  $\xi_{0,0}^R$  lead to improved performance in both surface-emitting efficiency and the quality factor. We speculate that this is because  $\xi_{0,0}^R$  directly influences the confinement factor ( $\Gamma_{\text{PhC}}$ ) within the photonic crystal, which in turn affects both the efficiency of surface-emitting power extraction and the quality factor. A higher  $\xi_{0,0}^R$  means a better confinement of light within the structure, leading to enhanced optical performance,

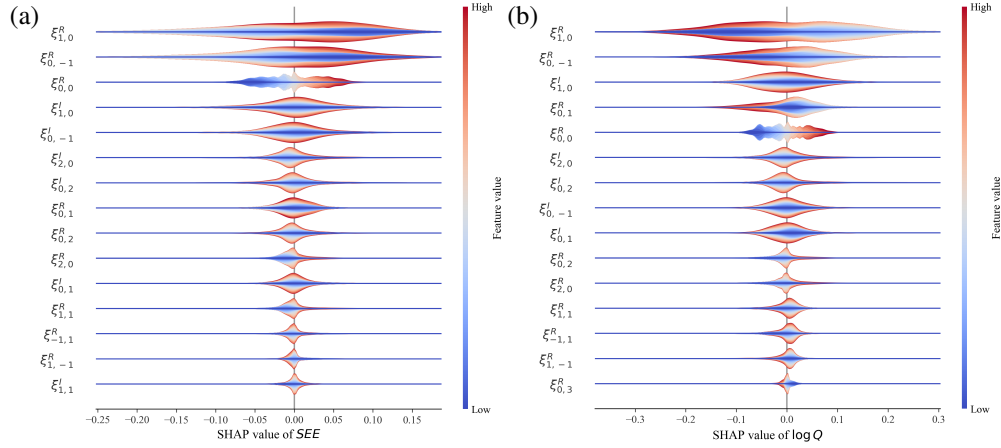


Fig. 3. SHAP (Shapley Additive Explanations) values for the top 15 most influential Fourier coefficients in predicting the  $SEE$  (a) and  $\log Q$  (b). Each row represents a Fourier coefficient, with the SHAP values shown along the x-axis. The color scale indicates the magnitude of the feature values, where red represents high values and blue represents low values. The violin plots show the distribution of SHAP values for each feature, highlighting its impact on the predicted  $SEE$  or  $\log Q$ . Positive SHAP values correspond to features that increase  $SEE$  or  $\log Q$ , while negative values correspond to features that decrease  $SEE$  or  $\log Q$ .

including higher  $SEE$  and  $\log Q$  values.

$\xi_{2,0}^R$  and  $\xi_{0,2}^R$  also exhibit a significant impact on both  $SEE$  and  $\log Q$ . It can be observed that when  $\xi_{2,0}^R$  and  $\xi_{0,2}^R$  are relatively low, both  $SEE$  and  $\log Q$  tend to decrease.

Other Fourier coefficients also contribute to the results, but their influence is less straightforward, indicating that there are complex interactions between them.

Table 3. Summary of the influence of Fourier coefficients on surface-emitting efficiency ( $SEE$ ) and the quality factor ( $\log Q$ ). The symbols "+" and "-" indicate positive and negative correlations, respectively. The number of "+" or "-" symbols represents the magnitude of the influence, with more symbols indicating a stronger effect on  $SEE$  and  $\log Q$ . "0" indicates no significant impact.

Feature	Impact on $SEE$	Impact on $\log Q$
$ \xi_{1,0}^R - \overline{\xi_{1,0}^R} $ and $ \xi_{0,1}^R - \overline{\xi_{0,1}^R} $	+++	---
$\xi_{0,0}^R$	++	++
$\xi_{2,0}^R$ and $\xi_{0,2}^R$	+	+
$\xi_{1,1}^R$	+	0
$\xi_{1,-1}^R$	-	-

#### 4. Conclusion

In this work, we developed a photonic crystal simulation framework based on Coupled-Wave Theory (CWT) to analyze and optimize the performance of Photonic Crystal Surface-Emitting

Lasers (PCSELS). By systematically modeling the interaction of optical waves within a structured photonic lattice, we derived key performance metrics, including surface-emitting efficiency ( $SEE$ ) and the quality factor ( $Q$ ). To further enhance the design process, we implemented a neural network model trained on a large dataset of simulated PCSEL structures. of the photonic crystal, enabling rapid optimization of device performance.

Additionally, we employed Shapley value analysis to interpret the contributions of different Fourier components, providing insights into the structural features that most significantly impact laser efficiency. Our results demonstrate that machine learning can serve as a powerful tool for guiding photonic crystal design, accelerating the discovery of high-performance PCSEL configurations. The methodology proposed in this study is flexible and can be extended to different epitaxial structures and laser designs, paving the way for future advancements in high-efficiency surface-emitting lasers.

**Funding.** This research was supported by the National Natural Science Foundation of China (NSFC) under Grant No. 62174144, the Shenzhen Science and Technology Program under Grants No. JCYJ 20220818102214030, No. KJZD20230923115114027, No. JSGG20220831093602004, No. KJZD 20240903095602004, the Guangdong Key Laboratory of Optoelectronic Materials and Chips under Grant No. 2022KSYS014, the Shenzhen Key Laboratory Project under Grant No. ZDSYS201603311644527, the Longgang Key Laboratory Project under Grants No. ZSYS2017003 and No. LGKCZSYS2018000015, and the Innovation Program for Quantum Science and Technology (Grant No. 2021ZD0300701), Hefei National Laboratory, Hefei 230088, China.

**Acknowledgment.** The authors would thank Ms. Floria Chen and Ms. Chuanyi Yang for their mentorship and revision tips. The authors would also thank Mr. Qi Xin and Mr. Sixuan Mao for his suggestions on frameworks of artificial neural networks.

**Disclosures.** The authors declare no conflicts of interest.

**Data availability.** Parts of Data underlying the results presented in this paper are not publicly available at this time but may be obtained from the authors upon reasonable request. The dataset for the NN model is available Ref. [21].

**Supplemental document.** A supplemental document must be called out in the back matter so that a link can be included. For example, “See Supplement 1 for supporting content.” Note that the Supplemental Document must also have a callout in the body of the paper.

## References

1. S. Noda, M. Yoshida, T. Inoue, *et al.*, “Photonic-crystal surface-emitting lasers,” *Nat. Rev. Electr. Eng.* **1**, 802–814 (2024).
2. H. Huang, C. Yang, H. Li, and Z. Zhang, “Unveiling the potential of photonic crystal surface emitting lasers: A concise review,” *Semicond. Sci. Technol.* (2025).
3. W. Zhou and M. Pan, “The future of photonic crystal surface-emitting lasers,” *Appl. Phys. Lett.* **123**, 140501 (2023).
4. B. King, H. Wenzel, E. Kuhn, *et al.*, “Design of very-large area photonic crystal surface emitting lasers with an all-semiconductor photonic crystal,” *Opt. Express* **32**, 44945 (2024).
5. K. Ishizaki, M. De Zoysa, and S. Noda, “Progress in photonic-crystal surface-emitting lasers,” *Photonics* **6**, 96 (2019).
6. Y.-H. Hong, W.-C. Miao, W.-C. Hsu, *et al.*, “Progress of photonic-crystal surface-emitting lasers: A paradigm shift in LiDAR application,” *Crystals* **12**, 800 (2022).
7. W.-H. Hsieh, D.-H. Huang, T.-C. Chen, *et al.*, “Optimal waveguide structure for low-threshold InGaN/GaN-based photonic-crystal surface-emitting lasers,” *AIP Adv.* **14**, 45108 (2024).
8. M. Yoshida, M. De Zoysa, K. Ishizaki, *et al.*, “Double-lattice photonic-crystal resonators enabling high-brightness semiconductor lasers with symmetric narrow-divergence beams,” *Nat. Mater.* **18**, 121–128 (2019).
9. C.-J. Chang, L.-R. Chen, K.-B. Hong, *et al.*, “Photonic crystal surface emitting lasers with multiple-junction operating at high order waveguide mode,” *Discov. Nano* **19**, 182 (2024).
10. G. Alagappan, J. R. Ong, Z. Yang, *et al.*, “Leveraging AI in Photonics and Beyond,” *Photonics* **9**, 75 (2022).
11. Z. A. Kudyshev, A. V. Kildishev, V. M. Shalaev, and A. Boltasseva, “Machine learning–assisted global optimization of photonic devices,” *Nanophotonics* **10**, 371–383 (2020).
12. T. Asano and S. Noda, “Optimization of photonic crystal nanocavities based on deep learning,” *Opt. Express* **26**, 32704 (2018).

13. Q. Liu, T. Baghdasaryan, and H. Ottevaere, "Data-driven investigation of thickness variations in multilayer thin film coatings," *J. Physics: Photonics* **6**, 45020 (2024).
14. P. Wallisch, M. E. Lusignan, M. D. Benayoun, *et al.*, "Chapter 36 - neural networks part I: Unsupervised learning," in *Matlab for Neuroscientists (Second Edition)*, P. Wallisch, M. E. Lusignan, M. D. Benayoun, *et al.*, eds. (Academic Press, San Diego, 2014), pp. 489–500.
15. Z. Wang, X. Liu, P. Wang, *et al.*, "Continuous-wave operation of 1550 nm low-threshold triple-lattice photonic-crystal surface-emitting lasers," *Light. Sci. & Appl.* **13**, 44 (2024).
16. Y. Liang, C. Peng, K. Sakai, *et al.*, "Three-dimensional coupled-wave model for square-lattice photonic crystal lasers with transverse electric polarization: A general approach," *Phys. Rev. B* **84**, 195119 (2011).
17. Y. Liang, C. Peng, K. Sakai, *et al.*, "Three-dimensional coupled-wave analysis for square-lattice photonic crystal surface emitting lasers with transverse-electric polarization: Finite-size effects," *Opt. Express* **20**, 15945 (2012).
18. Y. Liang, "Three-dimensional coupled-wave theory for photonic-crystal surface-emitting lasers," Ph.D. thesis, Kyoto University (2014).
19. L. S. Shapley, *Notes on the N-person Game — II: The Value of an N-person Game* (RAND Corporation, 1951).
20. Y.-A. Wang and Y.-N. Chen, "What do position embeddings learn? An empirical study of pre-trained language model positional encoding," (2020).
21. "Odatasets," .
22. S. M. Lundberg and S.-I. Lee, "A unified approach to interpreting model predictions," in *Advances in Neural Information Processing Systems*, vol. 30 (Curran Associates, Inc., 2017).